Astronomy & Astrophysics manuscript no. aanda
August 9, 2022

The miniJPAS Survey: Detection of Double-core Lyα Morphology of Two High-redshift QSOs

P. T. Rahna[1,⋆], Z.-Y. Zheng[1,⋆⋆], A. L. Chies-Santos[2,1], Z. Cai[3], D. Spinoso[4], I. Marquez[5], R. Overzier[6], L. R. Abramo[7], S. Bonoli[4], C. Kehrig[5], L. A. Díaz-García[5], M. Pović[8,5], R. Soria[9,10], J. M. Diego[11], T. Broadhurst[12,13,14], R. M. González Delgado[5], J. Alcaniz[6], N. Benítez[5,14], S. Carneiro[15], A. J. Cenarro[16], D. Cristóbal-Hornillos[16], R. A. Dupke[6,17,18], A. Ederoclite[16], A. Hernán-Caballero[16], C. López-Sanjuan[16], A. Marín-Franch[16], C. Mendes de Oliveira[19], M. Moles[5,16], L. Sodré Jr.[19], K. Taylor[20], J. Varela[16], H. Vázquez Ramió[16], and JPAS team

[1] CAS Key Laboratory for Research in Galaxies and Cosmology, Shanghai Astronomical Observatory, CAS, Shanghai, 200030, China.
[2] Instituto de Física, Universidade Federal do Rio Grande do Sul (UFRGS), Av. Bento Gonçalves, 9500, Porto Alegre, RS, Brazil
[3] Department of Astronomy, Tsinghua University, Beijing 100084, Peopleés Republic of China
[4] Donostia International Physics Center, Paseo Manuel de Lardizabal 4, E-20018 Donostia-San Sebastian, Spain
[5] Instituto de Astrofísica de Andalucía (CSIC), P.O. Box 3004, 18080 Granada, Spain
[6] Observatório Nacional/MCTI, Rua General José Cristino, 77, São Cristóvão, CEP 20921-400, Rio de Janeiro, Brazil
[7] Departamento de Física Matemática, Instituto de Física, Universidade de São Paulo, Rua do Matão, 1371, CEP 05508-090, São Paulo, Brazil
[8] Ethiopian Space Science and Technology Institute (ESSTI), Entoto Observatory and Research Centre (EORC), Astronomy and Astrophysics Research and Development Department, Addis Ababa, Ethiopia.
[9] College of Astronomy and Space Sciences, University of the Chinese Academy of Sciences, Beijing 100049, China
[10] Sydney Institute for Astronomy, School of Physics A28, The University of Sydney, Sydney, NSW 2006, Australia
[11] Instituto de Féısica de Cantabria, CSIC-Universidad de Cantabria, E-39005 Santander, Spain
[12] Department of Theoretical Physics, University of the Basque Country UPV-EHU, 48040 Bilbao, Spain
[13] Donostia International Physics Center (DIPC), 20018 Donostia, The Basque Country and IKERBASQUE, Basque Foundation for Science, Alameda Urquijo, 36-5 48008 Bilbao, Spain
[14] Ikerbasque, Basque Foundation for Science, E-48013 Bilbao, Spain
[15] Instituto de Física, Universidade Federal da Bahia, 40210-340, Salvador, BA, Brazil
[16] Centro de Estudios de Física del Cosmos de Aragón (CEFCA), Plaza San Juan, 1, E-44001, Teruel, Spain
[17] Department of Astronomy, University of Michigan, 311 West Hall, 1085 South University Ave., Ann Arbor, USA
[18] University of Alabama, Department of Physics and Astronomy, Gallalee Hall, Tuscaloosa, AL 35401, USA
[19] Universidade de São Paulo, Instituto de Astronomia, Geofísica e Ciências Atmosféricas, Depto. de Astronomia, Rua do Matão, 1226, CEP 05508-090, São Paulo, Brazil
[20] Instruments4, 4121 Pembury Place, La Canada Flintridge, CA 91011, USA

August 9, 2022

ABSTRACT

Context. The Lyα emission is an important tracer of neutral gas in a circum-galactic medium (CGM) around high-z QSOs. The origin of Lyα emission around QSOs is still under debate which has significant implications for galaxy formation and evolution.
Aims. In this paper, we study Lyα nebulae around two high redshift QSOs, SDSS J141935.58+525710.7 at $z = 3.128$ (hereafter QSO1) and SDSS J141813.40+525240.4 at $z = 3.287$ (hereafter QSO2), from the miniJPAS survey within the AEGIS field.
Methods. Using the contiguous narrow-band (NB) images from the miniJPAS survey and SDSS spectra, we analyse their morphology, nature, and origin.
Results. We report the detection of double-core morphology in the Lyα images of two QSOs. The separations of the two Lyα cores are 8.7 kpcs (1.15″) and 9.9 kpcs (1.32″) with Lyα line luminosities of $\sim 3 \times 10^{44}$ erg s^{-1} and $\sim 6 \times 10^{44}$ erg s^{-1} for QSO1 and QSO2, respectively. The miniJPAS NB images show evidence of extended Lyα and CIV morphology for both QSOs and extended HeII morphology for QSO1.
Conclusions. These two QSOs may be potential candidates for new enormous Lyman alpha nebula (ELAN) found from the miniJPAS survey due to their extended morphology in the shallow depth and relatively high Lyα luminosities. We suggest that galactic outflows are the major powering mechanism for the double-core Lyα morphology. Considering the relatively shallow exposures of miniJPAS, the objects found here could be the tip of the iceberg of a promising number of such objects that will be uncovered in the upcoming full J-PAS survey, and deep IFU observations with 8-10m telescopes will be essential to constrain the underlying physical mechanism that is responsible for the double-cored morphology.

Key words. galaxies: formation – galaxies: high-redshift –quasars: emission lines – galaxies: ISM

1. Introduction

The Lyman-alpha line of neutral hydrogen (Lyα λ1215.67) at high-redshift is a powerful probe of the Epoch of re-ionization (EoR, e.g., Malhotra & Rhoads 2006; Fan et al. 2006; Dijkstra et al. 2011; Treu et al. 2013; Mesinger et al. 2015; Davies et al. 2018; Mason et al. 2018; Greig et al. 2019). It is a gas tracer in the circum-galactic medium (CGM) and intergalactic medium (IGM) and help to understand the IGM ionization state and galaxy properties. CGM is the gaseous component that regulates the gas exchange between the galaxy and the IGM. Both IGM and CGM are vast reservoirs responsible for fueling the star formation of galaxies. Therefore studying the CGM is crucial for understanding galaxy formation and evolution, especially at the early Universe. Moreover, the Lyα line can be used to trace circum-galactic gas around high redshift ($z > 2$) Quasars (QSOs) as Lyα halo or nebulae.

There are several phenomena proposed for the origin of Lyα emission, including photoionization by Active Galactic Nuclei (AGN, Haiman & Rees 2001; Geach et al. 2009; Cai et al. 2017), shock heating by galactic superwinds (Taniguchi & Shioya 2000), cooling radiation from cold-mode accretion (Haiman et al. 2000; Fardal et al. 2001; Furlanetto et al. 2005; Dijkstra & Loeb 2009; Goerdt et al. 2010; Faucher-Giguère et al. 2010; Rosdahl & Blaizot 2012) and resonant scattering of Lyα photons from star-forming galaxies or AGN in the embedded galaxies (Hayes et al. 2011; Steidel et al. 2011). However, the physical drivers responsible for the diffuse Lyα emission are still under debate.

The typical Lyα emission around QSOs is diffuse and characterised by very low surface brightness (SB) levels, e.g. an expected SB level for detecting Lyα emission around QSOs at $z \sim 3$ is 10^{-20} erg s^{-1} cm^{-2} arcsec^2 (Haardt & Madau 1996; Cantalupo et al. 2005; Rauch et al. 2008). Therefore, detecting the full extent of very faint Lyα emission is an extreme challenge and current facilities are still not capable of detecting such low SB levels. Several observational efforts have been made to search for diffuse Lyα around high redshift QSOs. Previous detections employ different techniques such as NB imaging (e.g., Francis & Bland-Hawthorn 2004; Hu & Cowie 1987), long-slit spectroscopy (e.g., Bunker et al. 2003; Heckman et al. 1991; North et al. 2012), or integral field spectroscopy (IFS, Borisova et al. 2016; Christensen et al. 2006) for the detection of Lyα emission around QSOs. Among those three techniques, IFS is more efficient in the wavelength coverage while often constrained in a much smaller field of view. Most of the large Lyα nebulae like enormous lyman alpha nebulae (ELANs, Cantalupo et al. 2014; Hennawi et al. 2015; Cai et al. 2017; Arrigoni Battaia et al. 2018) are detected by either long exposure NB stacking analysis (e.g., 18 hrs at the 4m-KPNO/MOSAIC-1.1; Cai et al. (2017), 10 hrs at the 10m-Keck/LRIS; Cantalupo et al. (2014) or using MUSE-IFU at the 8m VLT (e.g., 4.5hrs Arrigoni Battaia et al. 2018) to achieve a SB level of 10^{-19} erg s^{-1} cm^{-2} arcsec^2 to trace the extended diffuse emission.

The NB surveys are often taken in a wide field to efficiently detect the diffuse Lyα emission while are often limited by fixed redshift windows. The Javalambre-Physics of the Accelerated Universe Astrophysical Survey (J-PAS, Benitez et al. 2014), is a multi-band survey with 54 NB (and 5 BB) filters. Because of its large field of view, the sub-arcsec spatial resolution, and contiguous NB filters acting as low-spectral resolution IFU, it is an ideal survey to study the diffuse Lyα emission around high-redshift QSOs.

In this paper, we present the detection of double-cored Lyα morphology of 2 high-z QSOs in the miniJPAS survey (Bonoli et al. 2021). MiniJPAS is a 1 deg^2 NB photometric survey on the AEGIS field, a proof-of-concept survey of the larger J-PAS project, which will soon start mapping thousands of deg^2 of the northern sky in 59 bands (54 NBs and 5 BBs, Bonoli et al. 2021). This paper is structured as follows. We introduce the sources and the JPAS and miniJPAS observations in Section 2. Analysis and results are presented in Section 3. A discussion on the physical properties and various powering mechanisms that contribute to the Lyα emission of the studied objects are given in Section 4. The main conclusion is presented in Section 5. We convert redshifts to physical distances (with a scale of 7.535 kpc/″ at $z = 3.218$ and 7.482kpc/″ at $z = 3.287$) assuming a ΛCDM cosmology with $\Omega_M = 0.3$ and $\Omega_\Lambda = 0.7$ and $H_0 = 70$ km s^{-1} Mpc^{-1}. All magnitudes are in the AB system.

2. Observation and Data

2.1. J-PAS and mini-JPAS surveys

The Javalambre-Physics of the Accelerated Universe Astrophysical Survey (J-PAS, Benitez et al. 2014) is a wide-area photometric survey soon to be conducted at the Javalambre Astrophysical Observatory (OAJ), located at the Sierra de Javalambre (Teruel, Spain). J-PAS will obtain a deep, sub-arcsec spectrophotometric map of the northern sky across 8000 deg^2. The survey will use the 2.5 m JST/T250 telescope and obtain multi-band imaging in optical bands with an effective field of view of 4.2 deg^2 and a plate scale of 0.225 arcsec pixel^{-1}. The J-PAS filters provide low-resolution spectroscopy (resolving power, R $\sim$ 60; which is also referred as J-spectra in this paper) of a large sample of astronomical objects with 54 NB filters (3780 to 9100 Å; $\Delta\lambda$= 145 Å), one blue medium-band (MB) filter (3497 Å; $\Delta\lambda$= 509Å), one red MB filter (9316 Å; $\Delta\lambda$= 635Å), and 3 SDSS Broad-Band (BB) filters. J-PAS nominal depth at signal-to-noise (SNR)$\sim$ 5 is between 22 to 23.5 AB mag for the NB filters and 24 for BB filters Bonoli et al. (2021). With a large set of NB filters, J-PAS makes it suitable for an extensive search for extended Lyα emission around QSOs from redshifts $z = 2.11$ to 6.66. Meanwhile, the wide spectral coverage of the J-spectra can cover Lyα , SIV+OIV, CIV, HeII, CIII], CII, and Mg II at $z > 2$, which allows us to study the properties of high redshift QSOs.

The miniJPAS survey (Bonoli et al. 2021) observed four AEGIS (All-wavelength Extended Groth Strip International Survey; Davis et al. 2007) fields in 2018-2019 with the pathfinder camera and detected more than 60,000 objects in a total area of 1 deg^2. The miniJPAS survey demonstrates the capabilities and unique potential of the upcoming J-PAS survey (Hernán-Caballero et al. 2021; González Delgado et al. 2021; Martínez-Solaeche et al. 2021; Queiroz et al. 2022; Martínez-Solaeche et al. 2022; Chaves-Montero et al. 2022). More detail about the observation and data reduction of miniJPAS is given in Bonoli et al. (2021). We obtained the miniJ-PAS images, flux catalogs, filter curves, and all other instrument information of these QSOs from the J-PAS database (CEFCA archive)[1].

2.2. Source properties

With miniJPAS, we report two interesting QSOs, SDSS J141935.58+525710.7 (RA: 214.8983, Dec:

⋆ 7rehanrenzin@gmail.com
⋆⋆ zhengzy@shao.ac.cn

[1] http://archive.cefca.es/catalogues/minijpas-pdr201912

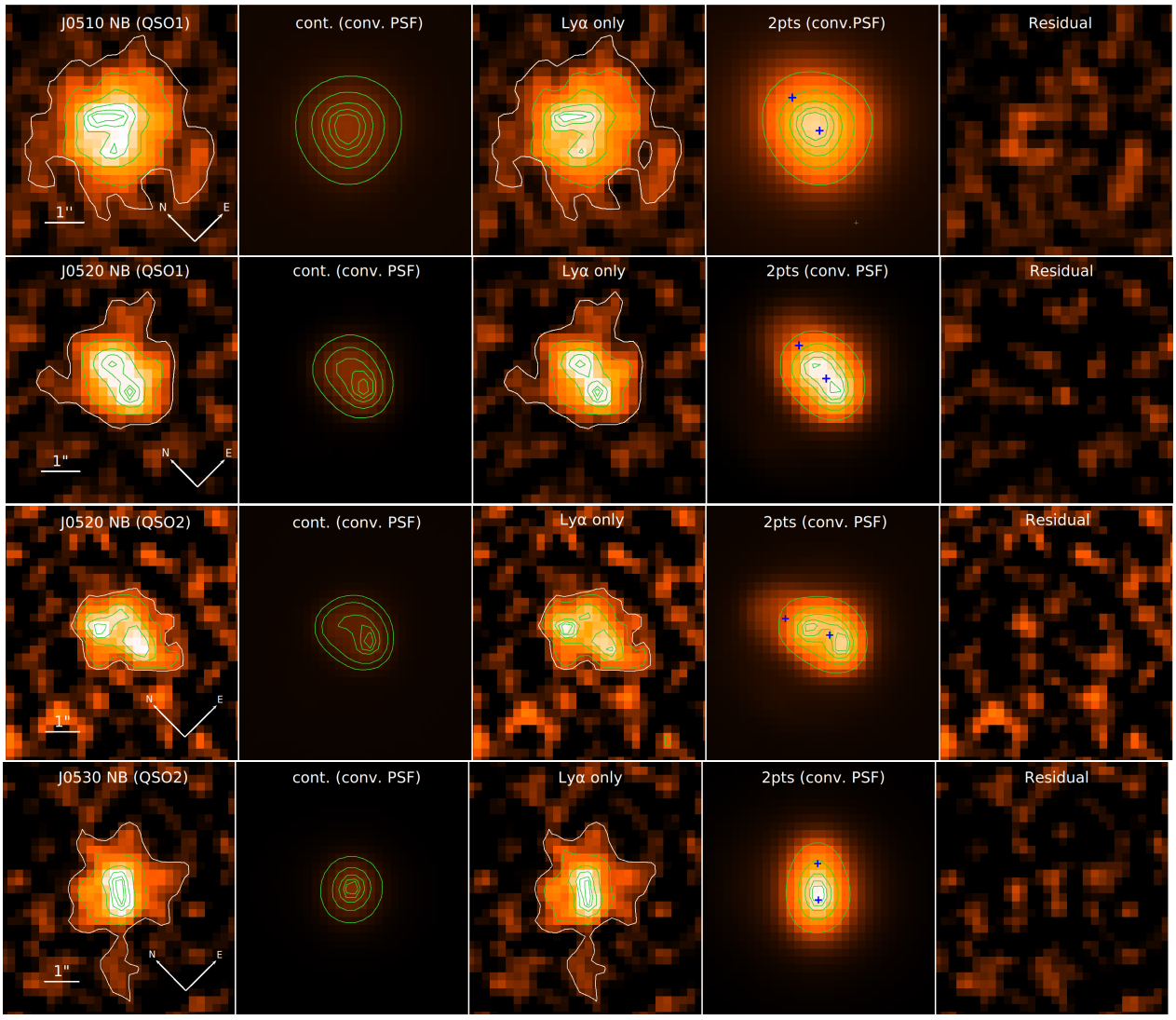

Fig. 1. QSO1 and QSO2 in two Lyα NB J-PAS filters: The 1st column shows NB miniJPAS image, 2nd column shows continuum image created by convolving PSF with continuum flux. 3rd column is the continuum subtracted Lyα image, 4th column is the PSFs in two points convolved with Lyα flux, 5th column shows the residual after subtracting 2 pts PSF from Lyα image. The Blue crosses represents the center of the PSF position given for GALFIT fitting, and the white contour in 1st and 3rd column represents an isophote of 2σ above the background STD. Green contours represent 30%, 60%, 80%, 90%, 95% of the peak values in the corresponding images.

52.953, hereafter QSO1) at redshift $z_{\rm spec}$ = 3.218 and SDSS J141813.40+525240.0 (RA: 214.5559, Dec: 52.8778, hereafter QSO2) at redshift $z_{\rm spec}$ = 3.287, with the double-core Lyα morphology (Fig. 1). We select these two QSOs in a systematic search on the Lyα nebulae around 59 (SDSS and miniJPAS cross matched targets) spectroscopically confirmed high redshift QSOs ($z > 2$) using miniJPAS (Rahna et al., in prep). Our target selection of Lyα nebulae is based on the excess of Lyα flux and morphology in filter covering Lyα line and continuum. Only these two targets from the parent sample show double-core morphology in their Lyα NBs. More details about the parent sample is explained in Rahna et al., in prep. Spectroscopic redshifts were available for these two QSOs thanks to SDSS/BOSS (Dawson et al. 2013; Pâris et al. 2017).

QSO1 has broadband observations with the Hubble Space Telescope (HST) Advanced Camera for Surveys (ACS/WFC) (AEGIS Survey; Davis et al. 2007). The HST/ACS F606W and F814W wide band images of QSO1 show a single point-like morphology. QSO1 is covered by a series of 31 Chandra observations taken between 2005 and 2008, for a total of about 800 ks. Both the AEGIS-X survey (Laird et al. 2009; Nandra et al. 2015) and the XDEEP2 survey (Goulding et al. 2012) used the same set of images classify the stacked image of QSO1 as a point-like source. However, this is not hugely constraining, because in all observations, QSO1 was located at ≈7 arcmin from the aimpoint of ACIS-I: at that distance, the ACIS-I PSF is elongated and distorted, with a 50% radius of about 2 arcsec (= 50% of the counts fall within 2 arcsec). Combine this large PSF with the moderately small number of counts (about 500 counts in the stacked image), it means that some faint, extended X-ray structure on scales <2 arcsec would be easily missed, especially with automated classifications of sources in large surveys. The radio observation of QSO1 with VLA in 6cm band (Ivison et al. 2007) shows weak but single-source detection. QSO2 has not been observed by HST, Chandra, XMM nor VLA.

3. Results

Here we discuss the analysis and results of the detection of the double-core Lyα morphology of the two high-redshift QSOs.

In Section 3.1, we introduce the detection of the double-core Lyα nebulae in the miniJPAS survey. We then compare the J-spectra with available SDSS spectra of the two QSOs in Section 3.2. We calculate the emission line luminosities and line ratios of the two QSOs in Section 3.3.

3.1. Detection of spatially resolved double-core morphology in Lyα NB images

The NB images covering the Lyα line for the QSOs analysed in this paper show a serendipitous double-cored morphology of Lyα (Fig. 1). The redshifted Lyα emission lines of the two QSOs fall into two NBs of J-PAS (J0510 and J0520 for QSO1 and J0520 and J0530 for QSO2). QSO1 shows features of double core morphology in both Lyα images, albeit more significant in J0520. QSO2 shows double-core morphology only in J0520. This may be due to the fact that J0530 covers mostly the NV line of QSO2 and the NV contamination may cause different morphology. Furthermore, J0530 also shows an elongated core at the center with extended morphology compared to the compact and circular PSF. On the other hand, the continuum image only shows a compact single-core morphology. We find that the double-core morphology is not caused by the PSF although it is elongated in the J0520 image. Nearby stars show elongated (same as single PSF in Fig. 1) but single-core morphology. Based on the morphology in the continuum bands, especially the single point structures revealed in HST F606W and F814W images, we infer that the double-core structures in the J0520 image of the two QSOs are caused by the diffuse and resonant-scattered Lyα radiation.

To quantitatively analyse the double-core morphology of the Lyα image of the two QSOs, we model the double-core with two PSF profiles through GALFIT (Peng et al. 2002). Firstly, we subtract the continuum flux from the NB image by using a PSF scaled to the continuum flux (from nearby filters J0490 for QSO1 and JO500 for QSO2 covering the continuum) to create the Lyα only image. Note that the center of the distorted PSF (blue cross) in J0520 filter doesn't coincide with the peak of the Lyα emission. Then, we convolve the two PSFs with the Lyα flux and subtract it from the Lyα-only image to get the residual (Fig. 1). The contour levels of the model created with two PSFs clearly show the double-core morphology compared to the actual elongated single-core PSF. This demonstrates that the double-peak is not due to the PSF effects. Input and output parameters used for GALFIT fitting are given in Table 1. Two cores are separated by a distance of 8.67 kpc in QSO1 and 9.9 kpc by QSO2 and SB peak at 18 and 9 sigma level of background standard deviation (STD).

Besides the double-core morphology in the Lyα images, both QSOs also show diffuse and spatially extended Lyα radiation. The spatial extent was measured at 2σ isophote above the background STD (10^{-16} – 10^{-17} erg s^{-1} cm^{-2} arcsec^{2}) from each image (Fig. 2). Compared to the size of the QSOs in J0520 filter, QSO1 is more extended in J0510 with a size of $\sim$ 45.21 kpc, and QSO2 is more extended in J0530 with a size of $\sim$ 44.89 kpc. This may be due to the difference in the depth of the two filters (in Tabl 2). However, the current miniJPAS has limited ability to estimate the actual size of Lyα nebulae due to shallow observation depth (480 secs) and PSF effects.

3.2. J-spectra vs SDSS spectra

We present the J-spectra (pseudo spectra) and the SDSS spectra of our two QSOs in the upper panels of Fig. 2. The SDSS spectra are obtained from the final data release of Baryon Oscillations Spectroscopic Survey (BOSS; Dawson et al. 2013) in SDSS DR12 (Pâris et al. 2017). QSO1 had been observed many times as part of the SDSS reverberation mapping project (Hemler et al. 2019) (59 epochs from 2014 to 2020) and the spectrum in Fig. 2 is taken on March 19, 2019, and QSO2 spectrum was observed on June 6, 2013. In BOSS, the spectrum were observed through 2 arcseconds (diameter) fibers. The J-spectra in Fig. 2 is composed of the atmosphere-extinction corrected photometry (APER2-2″ diameter) of all J-PAS NB filters obtained from the CEFCA archive (López-Sanjuan et al. 2019). The prominent emission lines such as Lyα, SIV+OIV, CIV, HeII, and CIII] detected in SDSS are visible in J-spectra. The properties of these filters are presented in Table 2. The spectroscopic Lyα profile of each QSO shows an asymmetric double-peaked profile and is dominated by the red peak, which is consistent with the general picture of IGM and CGM absorption Gurung-López et al. (2020). The broadened Lyα profile indicates radiative transfer effects. The double peak in the CIV line of QSO1 is may be due to the presence of CIV broad absorption lines (BALs) with high outflow velocity (vmax = 3243 km/s: Hemler et al. 2019).

By utilizing miniJPAS contiguous NB imaging, we can study the emission line morphology in various wavelengths, as shown in Fig. 2. Note that other emission lines observed through the NB and BB images do not exhibit such prominent double-core structures as the Lyα image. In Table 2, we list the emission line filter properties, APER size used for estimating luminosity in Col. 11, and estimated emission-line luminosities from miniJPAS images and SDSS spectra. APER size is the spatial extent measured at 2σ isophote above the background STD from each image. In addition to Lyα, QSO1 also exhibits spatially extended emission in HeII (J0690), CIV (J0650) and, CIII (J0690) while QSO2 shows extended morphology in CIV (J0660) (Fig. 2). The UV-continuum emission line (e.g., J0500, J0740) and BBs (gSDSS, rSDSS, iSDSS) are $\sim$ 15kpc size in both QSO1 and QSO2 and do not show spatially extended emission as in Lyα and CIV. The extended PSF in some emission line filters also contributes to the extended morphology. The comparison of 2σ contours on NB image (green) with PSF (white) in Fig. 2 shows how much nebula is extended in different emission lines.

3.3. Emission line luminosity and line ratios

To derive the emission line luminosities of the extended nebulae from miniJPAS images, we adopted a method that exploits contiguous narrow band filters of J-PAS. In this method, we use two adjacent NB filters covering the emission line and the adjacent continuum (by assuming that the source continuum is approximately constant in the nearest NB filter covering the continuum) to calculate continuum subtracted emission line fluxes. The emission line luminosity estimated from such flux is tabulated in Table 2. The spectral line widths of QSO1 and QSO2 are significantly wider than the filter width of J-PAS/miniJPAS NBs, which will result in a loss of flux in the luminosity calculated from miniJPAS images in a single filter comparison to SDSS spectra. The line luminosity calculated from SDSS spectra (by convolving J-PAS filter curves with SDSS spectra) and from miniJPAS NB images in the same aperture size of 2 arcsecs are within 1σ error limit (of L calculated from miniJPAS), except $L_{Ly\alpha}$, $L_{Ly\alpha\ +NV}$ in QSO1 and $L_{Ly\alpha\ +NV}$, L_{CIV} in QSO2. This variation might be due to the PSF effects. The luminosity estimated within the 2σ isophote size (col. 10) shows a significant increase in Lyα , SIV+OIV, CIV and HeII (weak) in QSO1 and Lyα in QSO2 as aperture size increases. Besides possible in-

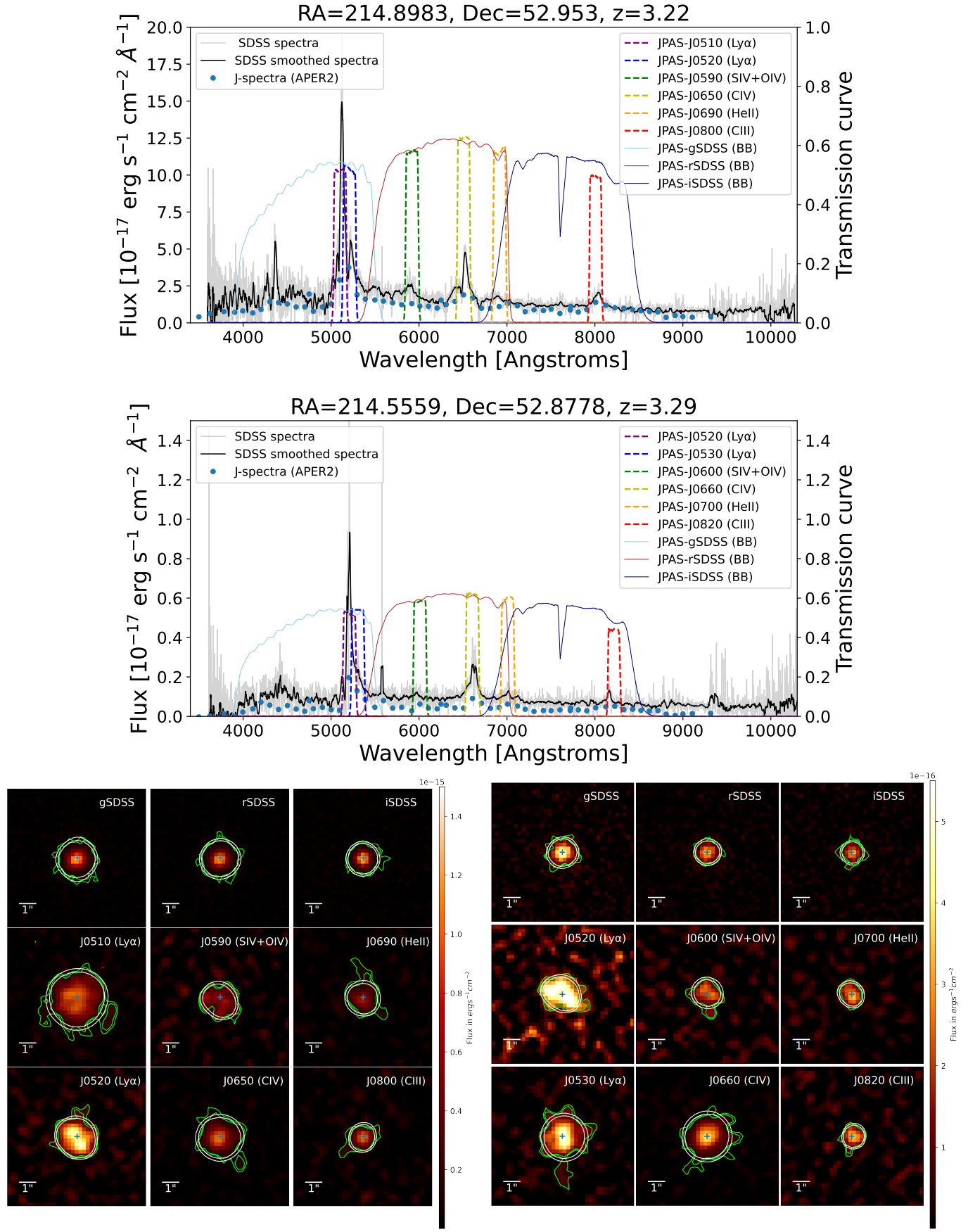

Fig. 2. Upper panel: SDSS spectra (Grey), Smoothed SDSS spectra (Black) and J-spectra (Blue dots) over-plotted with different NB and BB J-PAS filter curves covering the most prominent emission lines. Bottom panel: miniJPAS BB images (first row) and NB images (2 and 3rd row) of QSO1 (left) and QSO2 (right) covering the most prominent emission lines. The cross is the center of the QSO. All images are 12″ × 12″. The green (NB image) and white (PSF) contour levels represents isophote of 2σ, 3σ above the background STD of NB image. The center of the double-core coincides with the center of QSOs in BB filters

Table 1. Parameters for GALFIT PSF fitting

Source	Core	Position		Separation	Magnitude	χ^2	2σ	Peak	SB at peak
		RA (ICRS)	Dec(ICRS)	(″/kpc)	(mag)		(ADU)	(σ level)	(erg s^{-1} cm^{-2} arcsec^2)
QSO1-J0510	North Core	14:19:35.631	+52:57:12.064	1.15/8.67	21.65	0.792	0.0178	26	1.76×10^{-15}
	South Core	14:19:35.600	+52:57:10.721		19.75			25	1.69×10^{-15}
QSO1-J0520	North Core	14:19:35.631	+52:57:12.064	1.15/8.67	21.71	1.123	0.0284	17	2.97×10^{-15}
	South Core	14:19:35.600	+52:57:10.721		19.83			18	3.29×10^{-15}
QSO2-J0520	North Core	14:18:13.385	+52:52:41.162	1.32/9.88	20.42	1.067	0.0271	9	1.48×10^{-15}
	South Core	14:18:13.442	+52:52:39.952		22.00			9	1.48×10^{-15}
QSO2-J0530	North Core	14:18:13.486	+52:52:40.535	1.04/7.8	21.75	1.097	0.0124	21	1.1×10^{-15}
	South Core	14:18:13.413	+52:52:39.801		21.10			21	1.1×10^{-15}

Column (1): Filter name of the QSOs, Column (2-7): Cores, input PSF position in GALFIT, separation between two PSFs, best fit magnitude and χ^2 values from GALFIT fitting. Column (8-10): value of 2 σ (STD of background), the significance of the detection in σ level compare to the background level and corresponding SB values.

Table 2. Properties of the emission lines detected in the J-spectra of QSO1 and QSO2

Source	Em.line	λ_{Res}	J-PAS	λ_{eff}	$\Delta\lambda$	Depth	APER size		$L_{\lambda,APER2}$ (miniJPAS)	$L_{\lambda,2\sigma}$(miniJPAS)	$L_{\lambda,filtconv}$(SDSS)	$L_{\lambda,linespec}$(SDSS)
		(Å)	Filter	(Å)	(Å)	(mag)	(″)	(kpc)	(10^{43} erg s^{-1})	(10^{43} erg s^{-1})	(10^{43} erg s^{-1})	(10^{43} erg s^{-1})
QSO1	Lyα	1215.67	J0510	5097	148	24.37	6	45.21	24.04±2.08	71.87±5.69	37.15±0.39	62.41±0.64
	Lyα +NV	1215.67	J0520	5202	150	23.48	4	30.14	36.23±2.56	51.25±4.81	24.93±0.38	19.34±0.72
	SIV+OIV	1399.8	J0590	5917	152	23.39	3	22.61	2.57±1.74	8.59±2.54	3.84±0.31	...
	CIV	1549.48	J0650	6506	146	24.06	6	45.21	12.15±0.69	19.227±2.39	12.48±0.27	16.4±0.44
	HeII	1640.42	J0690	6912	148	23.75	4	30.14	1.26±0.98	2.45±2.05	1.35±0.25	1.77±0.32
	CIII]	1908.734	J0800	8009	140	22.89	3	22.61	4.55±1.47	5.54±2.29	4.07±0.198	6.76±0.37
QSO2	Lyα	1215.67	J0520	5202	150	23.48	3	22.45	23.59±2.12	37.16±3.09	23.05±0.38	28.13±0.57
	Lyα +NV	1215.67	J0530	5296	150	24.59	6	44.89	13.92± 1.32	26.78±2.94	11.29±0.37	12.27±0.82
	SIV+OIV	1399.8	J0600	6010	150	23.97	3	22.45	2.22±1.34	3.07±2.68	1.40±0.31	...
	CIV	1549.48	J0660	6607	151	24.97	4	29.93	7.32±0.76	10.45±1.52	10.08±0.26	13.52±0.63
	HeII	1640.42	J0700	7007	148	23.85	2	14.96	2.42±1.11	2.42±1.11	2.08±0.24	1.35±0.63
	CIII]	1908.734	J0820	8226	143	23.19	2	14.96	2.18±1.6	2.18±1.6	0.761±0.19	3.28±0.43

Column (1): Name of emission line, Column (2): rest-frame wavelength of emission line, Column (3-7): properties of J-PAS filters-filter name, effective wavelength, bandwidth, magnitude at SNR=5 in 1 square arcsec, Column (8-9): Aperture size of J-PAS catalog flux based on the size of 2σ isophote above background STD, Column (10-13): Line luminosity (L_λ) measured in APER2, 2σ isophote size from miniJPAS images and J-PAS filter curves convolved with SDSS spectra and total line luminosity given in SDSS BOSS spectra.

trinsic variability, the different line flux measurements may also contribute to the flux difference.

The relative strength of three important brightest UV emission lines such as Lyα, CIV, and HeII provide a powerful probe of the thermodynamic properties of the gas, its ionization state, gas density, and metallicity. These emission lines can also disentangle the powering mechanism for the Lyα emission. For example, line ratio diagnostic diagrams can be used to distinguish the photo-ionization scenario and shock scenario (e.g., Allen et al. 1998; Arrigoni Battaia et al. 2015). In the cooling zone behind high-velocity shocks, UV collisionally excited lines are strongly excited at high temperatures ($2 \times 10^4 - 10^5$ K), compared with photoionized plasmas, where these species are excited at 10^4 K (Allen et al. 1998). Therefore, UV line intensities are predicted to be much stronger in shock scenarios than in simple photo-ionization scenarios. Arrigoni Battaia et al. (2015) demonstrated the CIV/Lyα vs HeII/Lyα diagram as a method to discriminate between shock and photoionization models with strong upper limits calculated above 10^{-18} erg s^{-1} cm^{-2} arcsec^2 (at 2σ).

The line ratio of CIV/Lyα and HeII/Lyα are 0.262 ± 0.008, 0.028 ± 0.005 for QSO1 and 0.48 ± 0.024, 0.048 ± 0.022 for QSO2, which is estimated by the ratio of fluxes calculated from SDSS spectra. These values are consistent with the AGN photoionization (optically thick) and shock model for both QSOs explained by Arrigoni Battaia et al. (2015). But one needs to reach SB level of 10^{-18} to 10^{-19} erg s^{-1} cm^{-2} arcsec^2 at 2σ to trace the full extent of Lyα nebulae to discriminate these models. However, due to the limited depth (10^{-16} erg s^{-1} cm^{-2} arcsec^2 at 2σ) and spatial-spectral power of miniJPAS, we cannot constrain further details about different models. A deep J-PAS like NB surveys or IFU observation with 8-10m telescope would help to give a more definitive conclusion on this.

4. Discussions

In this section, we discuss the implications based on the results presented in the previous section. In Section 4.1. we discuss the size and luminosity relations of the Lyα nebulae around the two QSOs, and compare it with the literature candidates. We then discuss the physics behind the origin of the diffuse Lyα nebulae in Section 4.2 and origin of the double-core Lyα morphology in Section 4.3

4.1. $L_{Ly\alpha}$ vs. $Size_{Ly\alpha}$: Two New ELANs?

There is no clear definitions for different types of Lyα nebulae. It can be roughly classified into Lyα halos (LAH), Lyα blobs (LABs), and enormous Lyα nebulae (ELAN) based on their luminosity and size in the Lyα wavelength (Ouchi et al. 2020). LAHs are spatially extended Lyα nebulae with a physical scale of 1 to 10 kpc and a Lyα luminosity of $\sim 10^{42} - 10^{43}$ erg s^{-1} (Hayashino et al. 2004; Momose et al. 2014, 2016; Guo et al. 2020), LABs have a physical scale of ~ 10 -100 kpc and a luminosity of $10^{43} - 10^{44}$ erg s^{-1} (Steidel et al. 2000; Matsuda et al.

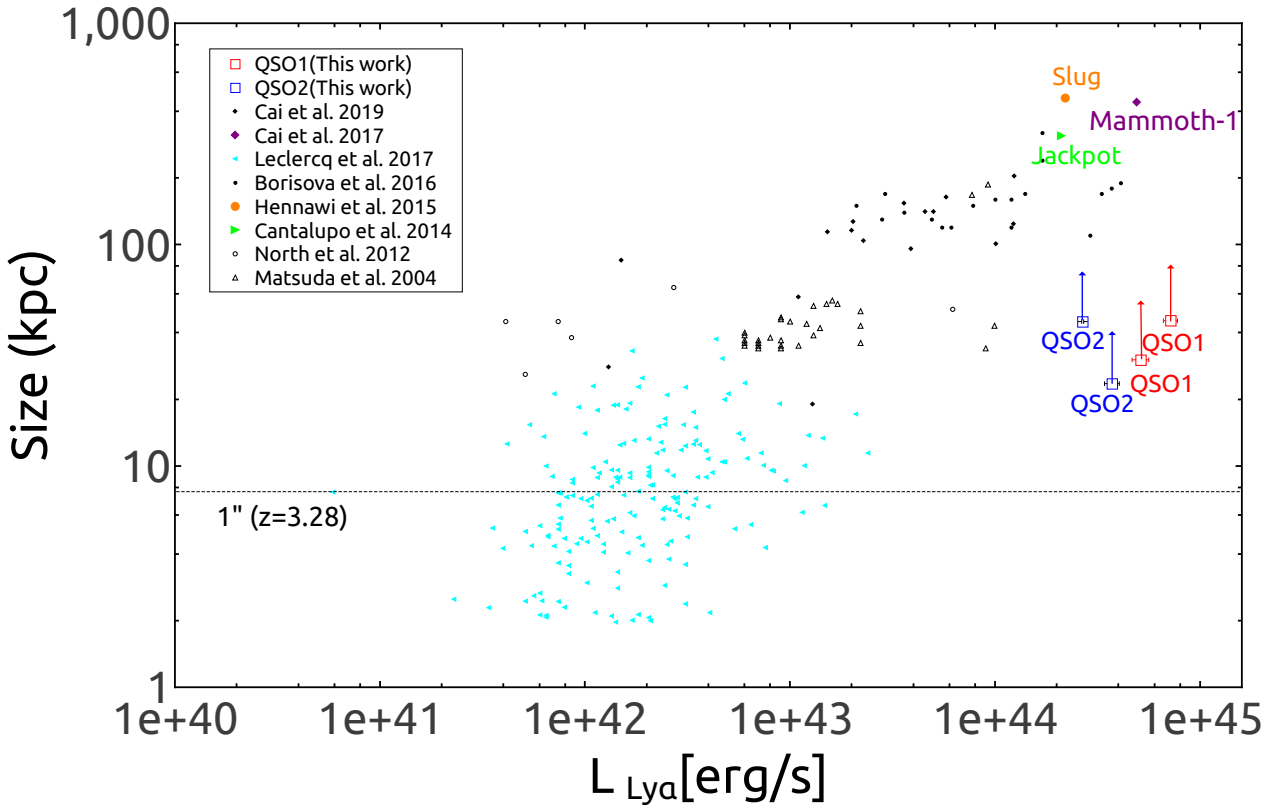

Fig. 3. Comparison of Lyα luminosity and size of the Lyα nebulae detected in this study with Lyα nebulae from the literature. Two square symbols of QSO 1 and 2 indicate two Lyα filters. LAHs are in cyan color, LABs are in black color and other color symbols are ELANs. All these Lyα nebulae are at high redshift ($z > 2$). Note that because of the different definitions of sizes, instrument sensitivity, methods, redshifts, the direct comparison between size and luminosity of the QSOs in this study with literature is not possible.

2004; Shibuya et al. 2018; Herenz et al. 2020) and ELANs are the most luminous ($> 10^{44}$ erg s $^{-1}$) and extend to a large scale of several hundreds of kpc (larger than the virial radius of dark matter halo) around $z > 2$ QSOs (Cantalupo et al. 2014; Hennawi et al. 2015; Cai et al. 2017; Arrigoni Battaia et al. 2018; Nowotka et al. 2022). Based on these classifications Lyα nebulae around two QSOs come under bright LABs with a Lyα luminosity of $\sim 3 - 6 \times 10^{44}$ erg s $^{-1}$ and physical size of $\sim 30 - 45$ kpc (Fig. 3). These QSOs are the most luminous and have a similar range of luminosity as ELANs (e.g., Slug, Jackot, MAMMOTH-1 in Fig. 3). Most importantly the spatial extent of the Lyα nebulae strongly depends on the limiting surface brightness. Kimock et al. (2021) demonstrated Lyα luminosity and enclosed area as a function of limiting surface brightness through high resolution cosmological zoom-in simulations. Comparing with their simulation results suggest that the current miniJPAS depth can only trace a small area near the center of nebulae and these two nebulae may be two new ELANs. Much deeper NB imaging are needed to confirm whether these objects are new ELANs.

4.2. Physics of the extended Lyα morphology

Here we discuss several mechanisms, including resonant scattering (e.g., Hayes et al. 2011; Steidel et al. 2011), gas photoionization by central AGN (e.g., Haiman & Rees 2001; Geach et al. 2009; Hayes et al. 2011), shocks due to gas flows (e.g., Taniguchi & Shioya 2000), cold gas accretion (e.g., Haiman et al. 2000; Fardal et al. 2001; Furlanetto et al. 2005; Dijkstra & Loeb 2009; Rosdahl & Blaizot 2012), which could be responsible for the extended Lyα emission around QSOs. A combination of all these mechanisms may also act together to power Lyα nebulae.

The morphology of rest-frame UV lines such as CIV λ1549 and HeII λ1640 along with Lyα provide additional information about different physical mechanisms explained in the previous section. For example, CIV/Lyα ratio provides a diagnostic for the halo gas metallicity and ionization state of halo gas in the CGM, while extended CIV morphology indicates the size of the metal-enriched halos from galactic outflows from central AGN (Arrigoni Battaia et al. 2015). Photoionization and galactic outflows are the two possible reasons for the Lyα emission if there is a detection of extended emission from both CIV and HeII lines. But the UV line ratios (e.g., CIV/Lyα and HeII/Lyα) are different in both scenarios. If the Lyα nebulae is powered by shocks due to galactic-scale outflows, shell-like or filamentary morphology with large Lyα width of $\sim$ 1000 km/s and enormous Lyα ($\sim$ 100 kpc) size is expected. Both QSOs have large Lyα width of $>$ 1000 km/s, suggesting that shell or filamentary like morphology could be expected for the extended Lyα emission surrounding them. However, the nominal depth of miniJPAS data cannot trace the extended size of these nebulae. Additionally, the NB covering the CIV emission line in both QSOs show extended morphology which suggests that the neutral gas expelled by outflows that are carbon (metal) enriched.

In gravitation cooling radiation, collisionally excited CGM gas emits Lyα photons and converts gravitational energy into thermal and kinetic energy as it falls into the dark matter (DM)

halo potential. The luminosity of Lyα nebulae produced by cooling radiation (in a 10^{11} DM halo) predicted to be $\leq 5{\times}10^{41}$ erg s $^{-1}$ through the hydrodynamic simulation of Dijkstra & Loeb (2009) and Rosdahl & Blaizot (2012). If Lyα nebulae has a luminosity higher than this value, it suggest that the mechanism producing Lyα emission is not only due to gravitation cooling radiation. Additionally, the powering mechanism for Lyα emission due to gravitational cooling radiation is not expected to produce extended CIV emission, but HeII emission can be expected (Arrigoni Battaia et al. 2015). This implies that the increased Lyα luminosity and extended CIV emission in both QSOs exclude a significant contribution from gravitational cooling.

Resonant scattering does not contribute to the large scale (> 100kpc) emission of Lyα nebulae because resonantly scattered photons can escape the system effectively only in very small scales (< 10kpc) (Dijkstra et al. 2006; Verhamme et al. 2006). Since CIV is a resonant line, the extended CIV emission in both QSOs could also arise due to the resonant scattering by the same medium scattering Lyα with non-detection in extended non-resonant HeII line. HeII does not have an extended structure in QSO2, but QSO1 has a faint extended emission signature in miniJPAS images. Therefore, the extended emission for HeII in QSO1 may be powered by a different scenario.

The double-peaked line profile in Lyα spectrum of QSOs at high redshift is common due to the resonant nature of Lyα (Dijkstra et al. 2006; Tapken et al. 2007; Yang et al. 2014; Cai et al. 2017). The Lyα line profile shows asymmetric due to the bulk motion of neutral hydrogen and Lyα photons escape in a double-peaked line due to the high optical depth at the line center and it is absorbed and re-emitted in another direction (Sanderson et al. 2021; Dijkstra et al. 2007; Matthee et al. 2018). Consequently, Lyα photons diffuse spatially and also in frequency space. The double-peak profile in the Lyα emission line seen in the SDSS spectra of both QSO1 and QSO2 indicates that the Lyα emission is powered by resonant scattering. Lyα line of both QSOs are redshifted with respect to other emission lines suggests that the Lyα photons scatter through large-scale outflows (Steidel et al. 2011). The galactic outflows (inflows) would also lead to an enhanced red (blue) peak in the Lyα profile (Zheng & Miralda-Escudé 2002; Verhamme et al. 2006; Dijkstra et al. 2007; Laursen et al. 2011; Weinberger et al. 2018). Moreover, IGM resonant scattering causes the diminishing of the blue peak. Therefore, galactic outflows play a role in powering Lyα emission in both QSOs and show redshifted Lyα profile with enhanced red Lyα peak.

4.3. Origin of the double-core Lyα morphology

Here we briefly outline the physics underlying the different scenarios that may explain double-core morphology in Lyα emission.

Double-cored Lyα has been seen in some high-z radio galaxies, where it appears to be related to jet interactions (e.g., Overzier et al. 2001), but neither QSO1 nor QSO2 is a radio-loud galaxy.

Gravitational lensing is one of the scenarios that can explain the unusual morphology in QSOs (Walsh et al. 1979; Meyer et al. 2019). However, the single-core QSO continuum component in miniJPAS BB (e.g., rSDSS) and NB images (e.g., J0490 in QSO1 and J0500 in QSO2) lacks the evidence for lensed QSOs and the corresponding lensing galaxy as well as binary QSOs. The single point structure in the HST F606W and F814W images of QSO1 also disfavor the QSO lensing hypothesis. Ionization echoes are often seen from type 2 AGN/QSO, as the echoes were enlightened by the previously active but now inactive SMBH. AGN ionization echoes are fossil records of the rapid shutdown of luminous QSOs, are uncovered in low-z (z = 0.05 to 0.35) characterised by high-ionization gas extending more than 10kpc from AGN and show strong [OIII]λ 5007 emission powered by type 2 AGN (Schawinski et al. 2010; Keel et al. 2012, 2015; Schweizer et al. 2013). The two QSOs reported here are all type 1 QSOs. Since these two QSOs have broad emission lines in their spectra, and AGN counterparts, we can rule out the AGN ionization echoes hypothesis. The morphology of Lyα emission due to outflows strongly depends on the orientation of the outflow with respect to the line of sight. Outflows emerging from QSOs show double-lobed (bipolar) structure in their morphology if viewed perpendicular to the cone axis. The morphology of the miniJPAS Lyα image and line profile from SDSS spectra support the hypothesis that outflows in these two QSOs are contributing to the double-core Lyα morphology in the miniJPAS image. Alternatively, it is possible that high central HI column density and/or dust obscuration may be the reason for asymmetric double core structure in QSO2.

5. Conclusions

We uncovered double-cored morphology in the Lyα NB image of two QSOs: SDSS-J141935.58+525710.7 and SDSS-J141813.40+525240.0 at z = 3.218 and z = 3.287, respectively during the search for extended Lyα around high-z QSOs in the miniJPAS survey. Our results are summarized as follows:

- The separations of the two Lyα cores are 8.7 kpc (1.15″) and 9.9 kpc (1.32″) with Lyα line luminosities of $\sim 3.72 \times 10^{44}$ erg s $^{-1}$ and $\sim 7.19 \times 10^{44}$ erg s $^{-1}$ for QSO1 and QSO2, respectively.
- The Lyα luminosity places these Lyα nebulae at the high luminosity end in the Luminosity-size diagram of the few previous detection of ELANs, suggesting that deeper observations might reveal the large-scale ELAN structure of these two QSOs.
- The spatially distributed double-core morphology in Lyα images might be due to scattering of Lyα photons through galactic outflows in bi-conical structure.
- Both QSOs show spatially extended strong CIV emission (> 30 kpc) in miniJPAS images suggest that halo gas in both QSOs are metal-rich and powered by collisional excitation by shocks or photoionization by AGN. The presence of faint extended HeII emission in QSO1 indicates additional contribution from collisional ionization due to shocks.
- This pilot study demonstrates the capability of J-PAS/miniJPAS to identify a large number of Lyα nebulae candidates by looking at the morphology in the Lyα NB filter (and other CIV and HeII NB filters).

It is quite unique to discover such double-core Lyα morphology from relatively shallow NB imaging surveys such as miniJPAS which covers only 1 deg^2 of the sky. The curious Lyα morphology of these QSOs may shed new light on the origin of these type of nebulae. The future J-PAS (will covers 8000 deg^2) may discover many of such objects ($\sim$ 1 per deg^2), warranting this pilot project. With the current miniJPAS observation, it is very hard to draw a conclusion about the primary driving mechanism for the origin of Lyα emission. We are planning for deep and wide field spectroscopic observations to make a more definitive statement about the kinematics, ionization status, metallicity, driving mechanism and to trace the large scale low SB level diffuse region of Lyα emission. In a forthcoming paper, we discuss more

cases of extended Lyα emission around high-z QSOs detected in the miniJPAS survey. These studies demonstrate the capability of contiguous NB imaging like JPAS survey to study the high-z Lyα nebulae.

Acknowledgements

Z.Y.Z. acknowledges support by the National Science Foundation of China (12022303), the China-Chile Joint Research Fund (CCJRF No. 1906) and the CAS Pioneer Hundred Talents Program. RPT thanks the CAS President's International Fellowship Initiative (PIFI) (Grant No. E085201009) for supporting this work. ACS acknowledges funding from the Conselho Nacional de Desenvolvimento Científico e Tecnológico (CNPq) and the Rio Grande do Sul Research Foundation (FAPERGS) through grants CNPq-11153/2018-6, CNPq-314301/2021-6 and FAPERGS/CAPES 19/2551-0000696-9 and the Chinese Academy of Sciences (CAS) President's International Fellowship Initiative (PIFI) through grant E085201009.

R.P.T and Z.Y.Z thanks Shuairu Zhu, Fang-Ting Yuan, Ruqiu Lin, and Xiang Ji for their useful discussion during the preparations of the manuscript. R. P. T acknowledge Carolina Queiroz for sharing information about JPAS data base.

This paper has gone through internal review by the J-PAS collaboration. Based on observations made with the JST/T250 telescope and JPCam at the Observatorio Astrofísico de Javalambre (OAJ), in Teruel, owned, managed, and operated by the Centro de Estudios de Física del Cosmos de Aragón (CEFCA). We acknowledge the OAJ Data Processing and Archiving Unit (UPAD) for reducing and calibrating the OAJ data used in this work.

Funding for the J-PAS Project has been provided by the Governments of Spain and Aragón through the Fondo de Inversión de Teruel, European FEDER funding and the Spanish Ministry of Science, Innovation and Universities, and by the Brazilian agencies FINEP, FAPESP, FAPERJ and by the National Observatory of Brazil. Additional funding was also provided by the Tartu Observatory and by the J-PAS Chinese Astronomical Consortium.

L.A.D.G., C.K. and R.G.D., acknowledge financial support from the State Agency for Research of the Spanish MCIU through the "Center of Excellence Severo Ochoa" award to the Instituto de Astrofísica de Andalucía (SEV-2017-0709), and to PID2019-109067-GB100.

References

Allen, M. G., Dopita, M. A., & Tsvetanov, Z. I. 1998, ApJ, 493, 571
Arrigoni Battaia, F., Prochaska, J. X., Hennawi, J. F., et al. 2018, MNRAS, 473, 3907
Arrigoni Battaia, F., Yang, Y., Hennawi, J. F., et al. 2015, ApJ, 804, 26
Benitez, N., Dupke, R., Moles, M., et al. 2014, arXiv e-prints, arXiv:1403.5237
Bonoli, S., Marín-Franch, A., Varela, J., et al. 2021, A&A, 653, A31
Borisova, E., Cantalupo, S., Lilly, S. J., et al. 2016, ApJ, 831, 39
Bunker, A., Smith, J., Spinrad, H., Stern, D., & Warren, S. 2003, Ap&SS, 284, 357
Cai, Z., Fan, X., Yang, Y., et al. 2017, ApJ, 837, 71
Cantalupo, S., Arrigoni-Battaia, F., Prochaska, J. X., Hennawi, J. F., & Madau, P. 2014, Nature, 506, 63
Cantalupo, S., Porciani, C., Lilly, S. J., & Miniati, F. 2005, ApJ, 628, 61
Chaves-Montero, J., Bonoli, S., Trakhtenbrot, B., et al. 2022, A&A, 660, A95
Christensen, L., Jahnke, K., Wisotzki, L., & Sánchez, S. F. 2006, A&A, 459, 717
Davies, F. B., Hennawi, J. F., Bañados, E., et al. 2018, ApJ, 864, 142
Davis, M., Guhathakurta, P., Konidaris, N. P., et al. 2007, ApJ, 660, L1
Dawson, K. S., Schlegel, D. J., Ahn, C. P., et al. 2013, AJ, 145, 10
Dijkstra, M., Haiman, Z., & Spaans, M. 2006, ApJ, 649, 14
Dijkstra, M., Lidz, A., & Wyithe, J. S. B. 2007, MNRAS, 377, 1175
Dijkstra, M. & Loeb, A. 2009, MNRAS, 400, 1109
Dijkstra, M., Mesinger, A., & Wyithe, J. S. B. 2011, MNRAS, 414, 2139
Fan, X., Strauss, M. A., Becker, R. H., et al. 2006, AJ, 132, 117
Fardal, M. A., Katz, N., Gardner, J. P., et al. 2001, ApJ, 562, 605
Faucher-Giguère, C.-A., Kereš, D., Dijkstra, M., Hernquist, L., & Zaldarriaga, M. 2010, ApJ, 725, 633
Francis, P. J. & Bland-Hawthorn, J. 2004, MNRAS, 353, 301
Furlanetto, S. R., Schaye, J., Springel, V., & Hernquist, L. 2005, ApJ, 622, 7
Geach, J. E., Alexander, D. M., Lehmer, B. D., et al. 2009, ApJ, 700, 1
Goerdt, T., Dekel, A., Sternberg, A., et al. 2010, MNRAS, 407, 613
González Delgado, R. M., Díaz-García, L. A., de Amorim, A., et al. 2021, A&A, 649, A79
Goulding, A. D., Forman, W. R., Hickox, R. C., et al. 2012, ApJS, 202, 6
Greig, B., Mesinger, A., & Bañados, E. 2019, MNRAS, 484, 5094
Guo, Y., Maiolino, R., Jiang, L., et al. 2020, ApJ, 898, 26
Gurung-López, S., Orsi, Á. A., Bonoli, S., et al. 2020, MNRAS, 491, 3266
Haardt, F. & Madau, P. 1996, ApJ, 461, 20
Haiman, Z. & Rees, M. J. 2001, ApJ, 556, 87
Haiman, Z., Spaans, M., & Quataert, E. 2000, ApJ, 537, L5
Hayashino, T., Matsuda, Y., Tamura, H., et al. 2004, AJ, 128, 2073
Hayes, M., Scarlata, C., & Siana, B. 2011, Nature, 476, 304
Heckman, T. M., Lehnert, M. D., Miley, G. K., & van Breugel, W. 1991, ApJ, 381, 373
Hemler, Z. S., Grier, C. J., Brandt, W. N., et al. 2019, ApJ, 872, 21
Hennawi, J. F., Prochaska, J. X., Cantalupo, S., & Arrigoni-Battaia, F. 2015, Science, 348, 779
Herenz, E. C., Hayes, M., & Scarlata, C. 2020, A&A, 642, A55
Hernán-Caballero, A., Varela, J., López-Sanjuan, C., et al. 2021, A&A, 654, A101
Hu, E. M. & Cowie, L. L. 1987, ApJ, 317, L7
Ivison, R. J., Chapman, S. C., Faber, S. M., et al. 2007, ApJ, 660, L77
Keel, W. C., Lintott, C. J., Schawinski, K., et al. 2012, AJ, 144, 66
Keel, W. C., Maksym, W. P., Bennert, V. N., et al. 2015, AJ, 149, 155
Kimock, B., Narayanan, D., Smith, A., et al. 2021, ApJ, 909, 119
Laird, E. S., Nandra, K., Georgakakis, A., et al. 2009, ApJS, 180, 102
Laursen, P., Sommer-Larsen, J., & Razoumov, A. O. 2011, ApJ, 728, 52
López-Sanjuan, C., Varela, J., Cristóbal-Hornillos, D., et al. 2019, A&A, 631, A119
Malhotra, S. & Rhoads, J. E. 2006, ApJ, 647, L95
Martínez-Solaeche, G., González Delgado, R. M., García-Benito, R., et al. 2021, A&A, 647, A158
Martínez-Solaeche, G., González Delgado, R. M., García-Benito, R., et al. 2022, A&A, 661, A99
Mason, C. A., Treu, T., de Barros, S., et al. 2018, ApJ, 857, L11
Matsuda, Y., Yamada, T., Hayashino, T., et al. 2004, AJ, 128, 569
Matthee, J., Sobral, D., Gronke, M., et al. 2018, A&A, 619, A136
Mesinger, A., Aykutalp, A., Vanzella, E., et al. 2015, MNRAS, 446, 566
Meyer, R. A., Delubac, T., Kneib, J.-P., & Courbin, F. 2019, A&A, 625, A56
Momose, R., Ouchi, M., Nakajima, K., et al. 2014, MNRAS, 442, 110
Momose, R., Ouchi, M., Nakajima, K., et al. 2016, MNRAS, 457, 2318
Nandra, K., Laird, E. S., Aird, J. A., et al. 2015, ApJS, 220, 10
North, P. L., Courbin, F., Eigenbrod, A., & Chelouche, D. 2012, A&A, 542, A91
Nowotka, M., Chen, C.-C., Battaia, F. A., et al. 2022, A&A, 658, A77
Ouchi, M., Ono, Y., & Shibuya, T. 2020, ARA&A, 58, 617
Overzier, R. A., Röttgering, H. J. A., Kurk, J. D., & De Breuck, C. 2001, A&A, 370, L39
Pâris, I., Petitjean, P., Ross, N. P., et al. 2017, A&A, 597, A79
Peng, C. Y., Ho, L. C., Impey, C. D., & Rix, H.-W. 2002, AJ, 124, 266
Queiroz, C., Abramo, L. R., Rodrigues, N. V. N., et al. 2022, arXiv e-prints, arXiv:2202.00103
Rauch, M., Haehnelt, M., Bunker, A., et al. 2008, ApJ, 681, 856
Rosdahl, J. & Blaizot, J. 2012, MNRAS, 423, 344
Sanderson, K. N., Prescott, M. K. M., Christensen, L., Fynbo, J., & Møller, P. 2021, arXiv e-prints, arXiv:2110.10865
Schawinski, K., Evans, D. A., Virani, S., et al. 2010, ApJ, 724, L30
Schweizer, F., Seitzer, P., Kelson, D. D., Villanueva, E. V., & Walth, G. L. 2013, ApJ, 773, 148
Shibuya, T., Ouchi, M., Harikane, Y., et al. 2018, PASJ, 70, S15
Steidel, C. C., Adelberger, K. L., Shapley, A. E., et al. 2000, ApJ, 532, 170
Steidel, C. C., Bogosavljević, M., Shapley, A. E., et al. 2011, ApJ, 736, 160
Taniguchi, Y. & Shioya, Y. 2000, ApJ, 532, L13
Tapken, C., Appenzeller, I., Noll, S., et al. 2007, A&A, 467, 63
Treu, T., Schmidt, K. B., Trenti, M., Bradley, L. D., & Stiavelli, M. 2013, ApJ, 775, L29
Verhamme, A., Schaerer, D., & Maselli, A. 2006, A&A, 460, 397
Walsh, D., Carswell, R. F., & Weymann, R. J. 1979, Nature, 279, 381
Weinberger, L. H., Kulkarni, G., Haehnelt, M. G., Choudhury, T. R., & Puchwein, E. 2018, MNRAS, 479, 2564
Yang, Y., Zabludoff, A., Jahnke, K., & Davé, R. 2014, ApJ, 793, 114
Zheng, Z. & Miralda-Escudé, J. 2002, ApJ, 578, 33